

The storm-substorm relationship: Ion injections in geosynchronous measurements and composite energetic neutral atom images

G. D. Reeves and M. G. Henderson

Los Alamos National Laboratory, Los Alamos, New Mexico

Abstract. We have analyzed isolated and storm time ion injections using geosynchronous particles, energetic neutral atom (ENA) data, and *Dst*. There are both surprising similarities between the two classes of events as well as important differences that bear directly on the relationship between storms and substorms. The average geosynchronous ion responses during the growth phase, at onset, and in the ≈ 15 min following onset are nearly identical in intensity, spectral hardness, and temporal profile. ENA observations confirm that similarity and additionally show that the two classes of injections span nearly the same extent in local time. The two classes of injections differ primarily in the subsequent behavior of the ion fluxes. For the isolated injections the fluxes return to preevent levels within about an hour, and exhibit the expected westward drift and dispersion. For the storm time injections the fluxes remain elevated for at least several hours following the initial injection. Additionally, the ENA observations show new evidence that the region of new particle injections expands eastward (opposite to the ion drift direction) to encompass most of the nightside. Within 3 hours, ENA emissions are observed coming from most of the inner magnetosphere but have still not formed a symmetric, trapped distribution. Within those same 3 hours *Dst* decreased an average of 40 nT with the initial decrease observed in the same hour as the initial injection. The isolated injections did not produce a measurable *Dst* signature. These results show that despite many remarkable similarities, storm time ion injection events are different from isolated injection events

1. Introduction

Geomagnetic storms and substorms are commonly observed and are fundamentally important magnetospheric processes. On that point there is general consensus. The precise relationship between substorms and storms, however, is considerably more controversial. Chapman [1962] coined the term “substorm” specifically because it implied that substorms were the essential building block of storms. In the reductionist view, understanding substorms would lead directly to understanding storms. More recently, the relationship between storms and substorms has been questioned by a number of authors. [e.g., Iyemori and Rao, 1996; Kamide *et al.*, 1998; Reeves, 1994; Tsurutani and Gonzalez, 1987; Gonzalez *et al.*, 1994; McPherron, 1997].

In this study we examine one important physical process that is common to both storms and substorms, namely, the injection of energetic ions into the region of the magnetosphere inside geosynchronous orbit ($R \approx 6.6 R_E$). For this study we use in situ data from the synchronous orbit particle analyzer (SOPA) instrument on the Los Alamos National Laboratory (LANL) geosynchronous satellites [e.g., Reeves *et al.*, 1996; Belian *et al.*, 1992] and energetic neutral atom (ENA) images from the comprehensive

energetic particle pitch angle distribution/imaging proton spectrometer (CEPPAD/IPS) instrument on NASA’s Polar satellite [Blake *et al.*, 1995; Henderson *et al.*, 1997]. The in situ measurements provide detailed information such as the duration of the injection, the intensity of the fluxes, and the spectral hardness, but the in situ measurements represent only the conditions that are local to that satellite. The ENA images compliment the in situ data by showing large-scale transport and providing a global context.

We compare seven isolated ion injection events with seven storm time ion injection events. To do this comparison we use a standard one-dimensional superposed epoch analysis technique for the geosynchronous ion observations and a two-dimensional extension of the superposed epoch technique, which we refer to as “composite” imaging, for the ENA observations.

2. Selection of the Events

All data used in this study came from the year 1997, when both LANL geosynchronous and Polar ENA measurements were available and geomagnetic disturbances were moderate. We began by selecting events for which Polar and LANL both observed ion injections. Polar’s CEPPAD/IPS instrument does not discriminate between neutral atoms and charged ions.

Therefore ENA observations are only possible when Polar is in the open magnetic field lines of the polar cap where energetic ion fluxes are extremely low. Additionally, we restricted our observations to times when Polar was near apogee above the North Pole in order to assure that ENA observations were possible for at least 3 hours continuously and also to assure that the ENA line of sight was nearly perpendicular to the solar-magnetospheric (SM) equatorial plane. (The reason for the second condition will be described in more detail in Appendix A, which discusses the ENA “composite” imaging technique.)

Events were also selected on the basis of the condition that one of the LANL geosynchronous satellites was located near magnetic local midnight and observed an injection of energetic ions that were “dispersionless” in energy, indicating that the satellite was within the injection region [e.g., *Mauk and Meng*, 1983]. (We limit our discussion to ion injections since electrons, naturally, produce no ENA signature. However, all ion injections were accompanied by a near-simultaneous electron injection.)

Two classes of ion injection events were selected. The first were “isolated ion injections,” and the second were “storm time ion injections.” The isolated ion injections are all associated with isolated substorms as confirmed by examining the preliminary AE index and the Polar auroral images. However, we avoid the more commonly used term “substorm injection” because we wish to avoid any prejudice that term might imply when we examine the storm time injections. Our selection of the “isolated injections” required that there be no significant injection of ions or electrons observed in the hour preceding the event and that there be no intensifications of the injection or no new injections in the interval from 1 to 3 hours after the event.

In the selection of our “storm time ion injections” we again required that there be no significant injections of ions or electrons in the hour prior to the onset of activity. In this case, though, we looked for higher levels of geomagnetic activity and a distinct decrease in the *Dst* index, evidence of injection of energetic ions into the storm time ring current. While a number of episodes of ion injection occurred during each of our storm events, we focused our analysis on the first significant ion injection of the storm.

Seven isolated ion injection events and seven storm time ion injection events which met these criteria were selected for this study. These events are in no way “unusual” nor are they “ideal” cases. They are representative of the two sets of conditions during which ion injections take place, and they include variations from event to event

which can be expected from our rather broad definitions of “isolated” and “storm time.”

3. LANL Geosynchronous Ion Observations

Plate 1 presents an overview of the LANL geosynchronous ion observations for each set of events. Plate 1a shows one of the isolated ion injections. Five differential energy channels with lower-energy cutoffs ranging from 50 to 250 keV are plotted. The data shown here are 1-min averages, averaged over three telescope look directions and over several 10.24-s spins of the satellite [e.g., *Reeves et al.*, 1996]. The ion injection begins abruptly in all energy channels in the same 1-min interval, which we refer to as a dispersionless injection. For this event the onset of the injection occurred at 1444 UT on April 9, 1997, which we define as the $T=0$ epoch for our superposed epoch study.

In the hour prior to the injection the ion fluxes remained quiet and slowly decreased in amplitude, with larger decreases at higher energies. This is the classic growth phase “dropout” caused by the stretching of the magnetic field near midnight into a more taillike configuration [e.g., *Baker et al.*, 1978]. Although the injection onset was simultaneous in all the SOPA energy channels, the peak fluxes were observed sooner at higher energies. This is characteristic of observations made within but toward the western edge of the injection region. Ions injected further to the east will gradient-curvature drift westward to be observed by the satellite with some energy dispersion.

We also observe that the fluxes return to their preinjection levels more quickly for the higher energies with the 50-keV ions requiring nearly an hour to return to undisturbed levels. One hour is approximately half the drift period for a 50-keV ion. *Reeves et al.* [1990] have shown that the injection region is often quite limited in local time and that therefore the duration of the injection pulse cannot be explained by drift alone but must also represent some continuing injection of energetic particles.

Plate 1b presents a single ion energy channel (75-113 keV) for all seven of our isolated injections. Also shown is the average flux profile over the seven events determined from a superposed epoch analysis. One can see that although there is a reasonable amount of variation in the detailed flux profiles for each of the seven isolated injection events, the superposed epoch fluxes share the features seen in Plate 1a. There is a modest decrease in fluxes during the growth phase (which can be more or less pronounced in

the individual events) followed by a rapid injection and a slower return to flux levels near their preinjection values within ~ 1 hour.

To compare with the isolated injections, Plates 1c and d present similar data for the storm time injections. Plate 1c shows a storm time injection that took place at 1710 UT on May 1, 1997. The growth phase dropout of the ion fluxes is similar to that seen prior to the isolated injections. Likewise, the abrupt increase in ion fluxes at the onset of the storm time injection is similar to the isolated injections. In the superposed epoch analysis shown in Plate 1d we again see that there is a reasonable amount of variation from one event to another but that before and in the initial stages of the injection, the superposed epoch fluxes for the storm time injections (Plate 1d) are again very similar to the superposed epoch fluxes for the isolated injections (Plate 1b). Not only are the shapes of the curves similar but, importantly, the magnitudes of the fluxes are also nearly identical.

Where the storm time injections differ significantly from the isolated injections is in the behavior following the initial 15 min of the injection. Rather than decreasing back to preinjection levels, the storm time ion fluxes remain elevated for several hours and may show considerable variation over that time. In other words the ion fluxes show evidence of ongoing geomagnetic activity and ongoing injection of ions into the region near geosynchronous orbit. It is important to note that the ongoing injection activity can either be episodic or apparently continuous. The evidence for continuous injection are the elevated fluxes that show no significant new enhancements of the flux (such as Plate 1c from epoch times 60-120 min. Continuous injection suggests that during those intervals a strong quasi-steady cross-tail electric field is more likely to be the cause of the transport than periodic stretching and collapse of the magnetic field. The episodic injections which seem to be superposed on the already high flux levels are more similar to the isolated injections that are associated with magnetotail stretch and collapse but also show some differences. One difference is that they tend to be more peaked, more frequent, and of shorter duration than isolated injections, often with no "growth phase" between them. Another important difference is that simultaneous observations from two closely spaced satellites often show that there are dispersionless injections observed at both local times but that they are uncorrelated with one another. That is not the case for the first injection of a storm, which is one of the reasons why we chose the first injection as the zero epoch for our analysis.

Plate 2 shows the results of our superposed epoch analysis for the first five SOPA proton channels. The storm time injections are shown in red, and the isolated injections are shown in purple. Both sets of curves are plotted on the same scale so that both relative and absolute flux comparisons can be made. We see that the remarkable similarity between the average fluxes during the growth phase dropouts is observed in all five energy channels. Likewise, the initial increase in fluxes at the onset of the injections is also remarkably similar. It is important to note that the initial injection of the storms is not more intense nor is it more energetic. In fact, in the first 15 min following the injection onset, the isolated injections have comparable or higher peak fluxes than the storm time injections. This is particularly true at the higher energies, suggesting that, on average, the isolated injections may actually be more energetic (i.e. spectrally harder) than the initial injection of a storm.

Again, Plate 2 shows that it is in the longer-term behavior that the isolated and storm time fluxes differ significantly. The storm time fluxes continue to increase for at least 60 min following the initial onset and often show peaks superposed on a more gradual rise. The higher-energy fluxes show more episodic variation both in the individual events and in the superposed epoch fluxes. The higher-energy fluxes also begin to decrease sooner than the lower-energy fluxes. At 50 keV the storm time fluxes remain elevated above the preinjection levels for at least 3 hours while the 250-keV fluxes return to preinjection levels within ~ 2 hours.

4. Ring Current Response

Since we have classified our events as storm time or isolated injections it is natural to check the ring current responses as measured by the *Dst* index. We do so in Plate 3 which shows the 1-hour *Dst* index for each of the events and the average *Dst* response for the isolated injections (Plate 3a) and for the storm time injections (Plate 3b). In each case the zero epoch time is chosen as the onset time for the injection events without reference to the behavior of the *Dst* index itself. We plot a time interval ranging from 4 hours before to 24 hours following the injection onset.

We see that for the isolated injection events (Plate 3a) there is no appreciable change in the *Dst* index in either the individual (colored) curves for each event or in the average (black) response for that class of events. This suggests either that (1) the isolated injection events do not effectively inject ions into the ring current or that (2) substorm current systems effectively cancel the *Dst* response [e.g., Rostoker et al., 1997] during

isolated injections but not during the first injection of a storm.

For the storm time injection events (Plate 3*b*) the minimum Dst ranged from -49 nT for the November 14, 1997, storm to -130 nT for the October 10, 1997, storm. The superposed epoch analysis resulted in an average minimum Dst of -64 nT for these seven storms. The storm time injections were selected, in part, on the basis of a subsequent decrease in the Dst index, so it is not surprising to find that there is a significant Dst response for these events. What is more significant is that the first change in Dst occurred at our zero epoch and that within the first 3 hours of the storm, Dst decreased by ~40 nT on average. The timing shows that the initial injection does, in fact, signal the onset of the storm and that the first few hours of injection activity following that initial injection result in a substantial buildup of the ring current.

5. Composite ENA Images

The events in this study were selected such that the Polar satellite acquired good energetic neutral atom (ENA) images for at least 1 hour before to 3 hours after the injection events. Our previously published ENA images from Polar [e.g., Henderson *et al.*, 1997, 1999; Jorgensen *et al.*, 2000] have had rather low resolution owing to the fact that the CEPPAD/IPS instrument samples 9×32 “pixels” over the unit sphere. This resolution is sufficient to resolve the storm time ring current and even isolated substorm injections, but it is an impediment to detailed comparison. Higher resolution can be obtained by using models to “invert” the images to get the initial ion distribution that best agrees with the data [e.g., Roelof, 1987; Henderson *et al.*, 1999], but this is not practical for investigating processes whose physical descriptions are not yet well specified. The imager for magnetopause-to-aurora global exploration (IMAGE) satellite, which has extensive instrumentation for neutral atom imaging, was launched in March 2000, but it will be some time before it has observed a sufficient number of storms to make possible an analysis such as we present here.

To make a detailed comparison of the ENA signatures of isolated and storm time injections we use a two-dimensional extension of the superposed epoch technique that we refer to as “composite” ENA imaging. The basis for this technique is superposing several images taken from different viewing perspectives into a single, higher-resolution image of the average ENA emissions over the events. We first project the measured ENA fluxes in each “pixel” to the SM

equatorial plane. As the Polar satellite moves in its orbit and as the orbit precesses throughout the year, the region of the equatorial plane covered by each pixel changes. By superposing the images taken from different perspectives we produce an average, or composite, image of the ENA response. In order to avoid a lengthy digression here, we present the details of the composite ENA imaging technique in Appendix A. It is, however, important to note here that the images represent ENA flux, not equatorial ion densities. ENAs are produced through charge exchange with the neutral exosphere which drops off approximately exponentially with altitude [e.g., Rairden *et al.*, 1986]. Therefore an equal equatorial ion density will produce a stronger ENA flux at lower altitudes. We have not attempted to deconvolve that response at this time.

Plate 4 shows the results of the composite ENA imaging technique applied to the isolated injection events (Plates 4*a*-4*d*) and to the storm time injection events (Plates 4*e*-4*h*). We show ENA fluxes from the CEPPAD/IPS integral channel, which measures ENAs with all energies above ~20 keV. Each frame shows the ENA emissions averaged over the seven events. The SM equatorial plane is shown with the Sun to the left, magnetic midnight to the right, and dawn at the top. A circle with a radius of $6.6 R_E$ represents geosynchronous orbit. Each frame presents a 1-hour interval. Higher time resolution images (as low as several minutes) were produced, but these images capture the general behavior we wish to discuss here.

Plates 4*a* and 4*e* show the 1-hour interval prior to the onset of the injection. By choice, the hour prior to onset is quiet with very low ENA fluxes observed in each event. The CEPPAD/IPS instrument is sensitive to photons as well as ions and neutral atoms, but pixels that were contaminated with photon fluxes were removed prior to producing the images. This leaves blank (black) areas in the images both near the Earth and in the sunward direction. Blank areas do not represent regions of zero ENA flux. They represent regions where ENA observations were not possible.

Plates 4*b* and 4*f* show the injection onset and the hour following onset. For both the isolated injections and the storm time injections we see a clear brightening of the ENA fluxes in the region inside geosynchronous orbit. In both cases the injection is centered in the pre-midnight region and extends from local times near dusk to a few hours east of local midnight. Since 1 hour of data is shown in these images, some westward drift of the injected ions is included in these images, particularly at the higher energies. (For reference, the drift period for a 20-keV ion at

geosynchronous orbit is ~ 5 hours.) The important thing to note, though, is that in this first hour following the onsets the isolated and storm time injections look remarkably similar in spatial extent and in magnitude. This confirms but also extends the observations seen in the superposed epoch analysis of the geosynchronous ion fluxes.

Plates 4c and 4g show times 1-2 hours after the injection and Plates 4d and 4h show times 2-3 hours after the injection. For the isolated injections we see continued westward drift of the injected ions and a decrease in the intensity of the fluxes. By 2-3 hours after the isolated injection the ENA fluxes near local midnight are essentially at their preinjection levels, and the peak ENA emission region has moved from premidnight to prenoon and significantly diminished in intensity.

The ENA signatures 1-3 hours after the storm time injections are quite different from those of the isolated injections. The ENA fluxes actually intensify in the 1-2 hours after storm onset compared to the 0-1 hour interval. Peak ENA fluxes are observed over a broader range of local times, spanning nearly the entire nightside magnetosphere. Not only does the injection of energetic ions into this region continue (as was also seen in the in situ geosynchronous observations) but the eastward expansion, which is opposite to the direction of the gradient-curvature drift of the ions, shows that the spatial extent of the injection region also expands during this time.

In Plates 4d and 4h, showing 2-3 hours after the initial injection, we see that the trend in the storm time ENA fluxes continues. The peak ENA fluxes become even more intense, and the spatial extent of those peak fluxes spans an even greater range of local times. The eastern extent of the injection region continues to extend at least to dawn. The new ENA emissions in the dusk to noon quadrant are consistent with westward drift of the injected ions, as is also seen for the isolated injections. However, unlike the isolated injection case, the ENA emissions from the premidnight local time sector do not diminish, which is further evidence for the continued injection of ions across most of the nightside.

6. Discussion and Conclusions

We have analyzed isolated and storm time ion injections using in situ geosynchronous particle data, remotely sensed energetic neutral atom data, and the *Dst* index. We find that there are both surprising similarities between the two classes of events as well as important differences that bear directly on the relationship between storms and substorms.

Our superposed epoch analysis of isolated and storm time ion injections show that the growth phase dropout and the initial period of injection are nearly identical for the two classes of events. Because the growth phase dropout is a signature of the tailward stretching of the magnetic field near local midnight, the similarity of the magnitude, rate of change, and spectral behavior of the energetic ions prior to the injection onsets suggest that the behavior of the magnetic field near local midnight may be remarkably similar for the two classes of events.

Likewise, the injection onset and the fluxes in the first 15 min following the onset are remarkably similar for isolated injections and the first injection of a storm. The geosynchronous observations show that the injected ion fluxes are very similar for the two cases. It is often assumed that the storm time injections are more intense (higher fluxes) or more energetic (spectrally harder) than isolated injections. The geosynchronous observations show that this is not the case, at least for the first injection of a storm. Similarly, the ENA observations for the two classes of events again show that the intensities are similar but additionally show that the injection regions for the two classes of events span nearly the same extent of local time. Despite the remarkable similarity between the initial behavior of the isolated and storm time injections, there is a distinct difference in the *Dst* response. Plate 3 shows that for the storm time events there is a clear decrease in *Dst* within the first hour of the first injection onset (at epoch time $T=0$ to within the 1-hour resolution of the index). Within the first 3 hours after the initial storm time ion injection, *Dst* decreased by ~ 40 nT on average. There is no similar decrease seen in the *Dst* index for the isolated injections.

Clearly, the storm time injections more effectively inject ions into the ring current than isolated injections do, even in the initial injection. This suggests (although it does not prove) that the injection of ions into the ring current is not simply the result of the superposition of a sequence of the type of injection seen in isolation (the classic "substorm injection").

Our results are consistent with those of *Iyemori and Rao* [1996], who examined the effect on *Dst* from substorms that occurred during the recovery phase of magnetic storms. The choice of the recovery phase is appropriate because during those times, individual substorms (and individual substorm injections) can be unambiguously identified. Iyemori and Rao concluded that the substorms had no measurable effect on *Dst*, which is consistent with what we found for the isolated injections (which occur during isolated substorms). In other words, the recovery phase

substorms are essentially the same as isolated substorms. Whether one chooses to associate the storm time injection events with “substorms” or not, it is clear that they are somehow different.

If the isolated and storm time injections are so similar in peak intensity, spectral hardness, and local time extent in the initial hour following the injections, how do we account for the difference in the *Dst* response? One difference, as Plate 2 shows, is that there is ongoing injection into the inner magnetosphere during the first hour of the storm intervals that is not generally present in the isolated injections. There appears to be both quasi-steady transport and new impulsive injections, which we suspect are associated with the quasi-steady convection electric fields and the more frequent occurrence of localized inductive electric fields that are present during geomagnetic storms. One can also speculate that a stronger convection electric field may inject ions to lower altitudes, where they can be more effectively trapped and can produce stronger ground magnetometer signals. While there may be some evidence for this in the composite ENA images, we again emphasize that the interpretation of the radial profiles must take into account both the radial profile of the neutral exosphere and the three-dimensional nature of the ENA emission region.

The conclusions which apply to the first hour after the initial injection continue to apply for up to 3 hours afterwards. At lower energies (e.g., 50 keV) the storm time geosynchronous ion fluxes remain elevated throughout this interval, and *Dst* continues to decrease. Interestingly, at higher energies (e.g., 250 keV) the geosynchronous fluxes for these storms peak and return to prestorm levels within about 2 hours even though *Dst* typically does not reach its minimum value for several hours to come. This suggests that at least for these storms there may be some difference in the plasma sheet source population in the early hours of the main phase of a storm compared to later times.

Another observation worth noting in the first 3 hours of the storms that differs significantly from the isolated injections is the eastward expansion of the injection region. Unlike the western boundary of the ENA emissions which expands, at least partly, because of the westward drift of previously injected ions, the eastern expansion is unambiguously an expansion of the local time extent of ongoing injection activity, which, to our knowledge, has not been previously reported.

Finally, we comment on the nature of the *Dst* index as a measurement of the ring current. Since the *Dst* index is produced through a synthesis of low-latitude to midlatitude ground magnetometer stations, it is, naturally, subject to effects from

current systems other than the ring current, such as the magnetopause current system, the cross-tail current, and the substorm current wedge [e.g., Turner *et al.*, 2000]. Energetic neutral atom emissions from the inner magnetosphere are largely insensitive to those other current systems and thus introduce the possibility of isolating the effect of those current systems on the *Dst* index. We have seen in this study that the decrease of the *Dst* index in the storm main phase begins with the first injection of ions and reaches more than half its (average) minimum value before the injected ions become even approximately symmetric in local time. This suggests that much of the *Dst* response during the main phase is from ions which may or may not become trapped, depending on the subsequent temporal evolution of the convection electric field. More generally, other studies have shown that there is a good correspondence between *Dst* and the overall ENA emission rate over a long period of time and a number of storms [Jorgensen *et al.*, 1997]. This suggests that the effects of non-ring current sources on *Dst* for those events are not a dominant effect. More detailed analysis of the relationship between *Dst*, ENA emissions, and in situ ion observations is in progress.

Appendix A

We now describe in more detail the construction of the “composite” ENA images. The Polar satellite is in an $\sim 2 \times 9 R_E$ orbit. During 1997 the apogee of Polar was at nearly 90° and Polar spent nearly half of its ≈ 18 -hour orbit at high latitudes on field lines devoid of energetic ions, where Energetic neutral atoms become the dominant source of counts in the IPS instrument.

For this study we were even more restrictive. We required that Polar be $\sim 8 R_E$ or higher above the SM equatorial plane ($Z_{SM} > 8 R_E$) at the onset of each event. This restriction was imposed for two reasons. First, we wanted to have ENA observations for at least 1 hour prior to injection onset and 3 hours after injection onset. (It is this limitation that prevents us from extending the analysis throughout the storm main phase.) Second, we wanted to have the viewing geometry nearly perpendicular to the equatorial plane. The magnetosphere is optically thin to ENAs, and charge exchanges occur throughout the three-dimensional volume of a flux tube. For a given flux tube, however, the majority of the ENA emissions come primarily from two regions. One is the low-altitude “horn” of the flux tube, where the neutral exospheric density is highest. Emissions from those regions appear to come from near the Earth regardless of the *L* shell of the

particular flux tube. The second region of high emission is where the line of sight is tangent to the flux tube. When the vantage point is at high Z_{SM} , the tangent points occur primarily near the equator.

Plate 5 provides a quantitative measure of the line of sight effect. Plate 5 shows the percentage of ENA emissions which come from the region within $1 R_E$ of the equatorial plane relative to the emissions from the entire magnetosphere along each particular line of sight. The ENA emissions are calculated theoretically using the Roelof 10-parameter model [e.g., Roelof *et al.*, 1993]. For reference, the equatorial plane with a $2 \times 2 R_E$ grid is superposed. At geosynchronous orbit ($6.6 R_E$) $\sim 50\%$ of the ENA emissions come from within $1 R_E$ of the equatorial plane. This increases to $\sim 75\%$ at $3 R_E$ and then decreases to less than 25% at very low L shells. The reason for the decrease at low L shells is that emissions from the low-altitude “horns” of the flux tubes become dominant. Plate 5 is calculated for an oblique perspective. When the line of sight is more perpendicular to the equatorial plane, the percentages originating near the equatorial plane become larger.

The assumption that the emissions for each event come from a common plane is an important assumption for producing a “composite” superposed epoch image, since we can then simplify the problem to a reconstruction of a two-dimensional image. Both the modeling and the end result of the reconstruction suggest that this is a valid and powerful technique if care is taken in the selection of the original images. Just as with a traditional linear superposed epoch analysis, the composite imaging also depends on the existence of a well-defined reference for the epoch time and a meaningful “average behavior” of the system.

The value of composite imaging for ENA observations is the possibility of improving spatial and/or temporal resolution. The field of view of each detector (or pixel) of the CEPPAD/IPS instrument is 20° by 11.25° , but the portion of the equatorial plane viewed by each pixel varies as Polar moves in its orbit and varies from event to event. We have chosen events throughout the year, so the precession of the Polar orbital plane provides a wide variety of viewing perspectives. Since the pixel sampling of the equatorial plane is varying, one can supersample that plane and average the ENA emissions from each point on the plane from each 16-s spin of the Polar satellite. With a sufficiently large number of images taken from random perspectives, very high resolution composite images can be obtained.

The technique is illustrated in Figure 1 for a more familiar image, a portrait of Abraham Lincoln. We began with a high-resolution (1500×1500 pixel) image of Abraham Lincoln

(courtesy of the United States National Archives). We then translated and rotated the image in nine different ways to produce nine unique image perspectives. For each perspective we then binned the image down to a resolution of 15×15 pixels. Figure 1a shows an example of one of the 15×15 images. Knowing that the original image was of Abraham Lincoln Figure 1a is recognizable as a person, but at this resolution no features are recognizable. Figure 1b is a composite of two images taken 45° with respect to each other. With only two images some facial features begin to be recognizable. Figure 1c is a composite of nine images. Now eyes, nose, and beard are clearly recognizable, and sharp boundaries such as the neck become clear even at relatively low contrast.

We have extended the results shown in Figure 1 by producing composite images with up to 45 individual low-resolution images (which we do not show here). While the sharpness of the features in the composite image continues to increase with the addition of each new image, the benefits from each additional image begin to decline after about a dozen images have been used. We found empirically that the ultimate resolution we obtained for this image was equivalent to the original image after applying Gaussian blur with radius $\sim 3\%$ of the original image dimensions.

We believe that this technique will be a powerful tool for neutral atom imaging, not only for low-resolution measurements from Polar, but also for the higher-resolution images that will soon be available from the IMAGE mission. With an appropriate choice of the subset of magnetospheric conditions and a sufficiently large number of images, it should be possible to obtain high spatial and temporal resolution images for the average magnetospheric conditions under different solar wind drivers, for different Kp levels, for high- and low-density plasma sheet intervals, and for many other distinguishable conditions.

Acknowledgments. We would like to thank R. D. Belian, J. B. Blake, and H. E. Spence for their years of work making the instruments that made this study possible. We thank the World Data Center in Kyoto for providing preliminary AE indices and the Polar VIS and UVI teams (especially L. Frank and G. Parks) as well as the CDAWeb development team for providing auroral image key parameters which were used in this study. This work was supported by NASA’s International Solar Terrestrial Physics Program (ISTP) and by the U.S. Department of Energy Office of Basic Energy Science (OBES).

Janet G. Luhmann thanks Walter D. Gonzalez and another referee for their assistance in evaluating this paper.

References

- Baker, D. N., P. R. Higbie, E. W. Hones Jr., and R. D. Belian, High-resolution energetic particle measurements at $6.6 R_E$, 3, Low-energy electron

- anisotropies and short-term substorm predictions, *J. Geophys. Res.*, **83**, 4864, 1978.
- Belian, R. D., G. R. Gisler, T. E. Cayton, and R. Christensen, High Z energetic particles at geosynchronous orbit during the great solar proton event of October, 1989, *J. Geophys. Res.*, **97**, 16,897, 1992.
- Blake, J. B., et al., CEPPAD: Comprehensive Energetic Particle and Pitch Angle Distribution experiment on Polar, *Space Sci. Rev.*, **71**, 531, 1995.
- Chapman, S., Earth storms: Retrospect and prospect, *J. Phys. Soc. Jpn.*, **6**, suppl. A-1, 17, 1962.
- González, W. D., J. A. Joselyn, Y. Kamide, H. W. Kroehl, G. Rostoker, B. T. Tsurutani, and V. M. Vasyliunas, What is a geomagnetic storm?, *J. Geophys. Res.*, **99**, 5771, 1994.
- Henderson, M. G., G. D. Reeves, H. E. Spence, R. B. Sheldon, A. M. Jorgensen, J. B. Blake, and J. F. Fennell, First energetic neutral atom images from Polar CEPPAD/IPS, *Geophys. Res. Lett.*, **24**, 1167, 1997.
- Henderson, M. G., G. D. Reeves, K. R. Moore, H. E. Spence, A. M. Jorgensen, J. F. Fennell, J. B. Blake, and E. C. Roelof, Energetic neutral atom imaging with the Polar CEPPAD/IPS instrument: Initial forward modeling results, *Phys. Chem. Earth*, **24**, 203, 1999.
- Iyemori, T., and D. R. K. Rao, Decay of the *Dst* field of geomagnetic disturbances after substorm onset and its implication to substorm relation, *Ann. Geophys.*, **14**, 608, 1996.
- Jorgensen, A. M., H. E. Spence, M. G. Henderson, G. D. Reeves, M. Sugiura, and T. Kamei, Global energetic neutral atom (ENA) measurements and their association with the *Dst* index, *Geophys. Res. Lett.*, **24**, 3173, 1997.
- Jorgensen, A. M., L. Kepko, M. G. Henderson, H. E. Spence, G. D. Reeves, J. B. Sigwarth, and L. A. Frank, The association of Energetic Neutral Atom (ENA) bursts and magnetospheric substorms, *J. Geophys. Res.*, **105**, 18,753, 2000.
- Kamide, Y., et al., Current understanding of magnetic storms: Storm/substorm relationships, *J. Geophys. Res.*, **103**, 17,705, 1998.
- Mauk, B. H., and C.-I. Meng, Characterization of geostationary particle signatures based on the injection model event, *J. Geophys. Res.*, **88**, 3055, 1983.
- McPherron, R. L., The role of substorms in the generation of magnetic storms, in *Magnetic Storms, American Geophysical Union Geophys. Monogr. Ser.*, Vol. 98, p. 131, AGU, Washington D. C., 1997.
- Rairden, R. L., L. A. Frank, and J. D. Craven, Geocoronal imaging with Dynamics Explorer, *J. Geophys. Res.*, **91**, 13,613, 1986.
- Reeves, G. D., Energetic particle observations at geosynchronous orbit, paper presented at International Workshop on Magnetic Storms, Solar Terr. Env. Lab., Rikubetsu, Japan, Oct. 6-8, 1994.
- Reeves, G. D., T. A. Fritz, T. E. Cayton, and R. D. Belian, Multi-satellite measurements of the substorm injection region, *Geophys. Res. Lett.*, **17**, 2015, 1990.
- Reeves, G. D., R. D. Belian, T. C. Cayton, R. A. Christensen, M. G. Henderson, and P. S. McLachlan, Los Alamos space weather data products: On line and on time, in *Substorms 3, Eur. Space Agency Spec. Publ.*, ESA SP-339, 689, 1996.
- Roelof, E. C., Energetic neutral atom image of a storm time ring current, *Geophys. Res. Lett.*, **14**, 652, 1987.
- Roelof, E. C., B. H. Mauk, R. R. Meier, K. R. Moore, and R. A. Wolf, Simulations of EUV and ENA magnetospheric images based on the Rice Convection Model, *Proc. SPIE 2008*, **202**, 1993.
- Rostoker, G., W. Baumjohann, W. Gonzalez, Y. Kamide, S. Kokubun, R. L. McPherron, and B. T. Tsurutani, Comment on "Decay of the *Dst* field of geomagnetic disturbance after substorm onset and its implication to storm-substorm relations" by T. Iyemori and D. R. K. Rao, *Ann. Geophys.*, **15**, 848, 1997.
- Tsurutani, B. T., and W. D. Gonzalez, The cause of high-intensity long-duration continuous *AE* activity (HILDCAAS): Interplanetary Alfvén wave trains, *Planet. Space Sci.*, **35**, 405, 1987.
- Turner, N. E., D. N. Baker, T. I. Pulkkinen, and R. L. McPherron, Evaluation of the tail current contribution to *Dst*, *J. Geophys. Res.*, **105**, 5431, 2000.

M. G. Henderson and G. D. Reeves, Los Alamos National Laboratory, NIS-1 MS D-466, Los Alamos, NM 87545. (reeves@lanl.gov)

(Received May 1, 2000; revised August 25, 2000; accepted August 25, 2000)

This paper is not subject to U.S. copyright. Published in 2001 by the American Geophysical Union.

Paper number 2000JA003017

Figure Captions

Plate 1. Geosynchronous ion observations. (a) An example of one of the isolated injections. The epoch time, $T_0=1444$ UT, is the time of a dispersionless ion injection. (b) A superposed epoch analysis of seven isolated injections. Only the 75-113 keV ion fluxes are shown. Individual injections are shown in color, and the average response is shown in black. (c) An example of one of the storm time injections. The epoch time, $T_0=1710$ UT, is the time of the first dispersionless ion injection of the event. (d) A superposed epoch analysis of seven storm time injections in the same format as that of Plate 1b.

Plate 2. Results of the superposed epoch analysis of geosynchronous ion fluxes for five different energy channels. Isolated injections are shown in purple and storm time injections are shown in red.

Plate 3. Superposed epoch analysis of the *Dst* index for (a) the isolated injections and (b) the storm time injections. In both cases the zero epoch time is determined from the geosynchronous injection time. *Dst* responses for the individual events are shown in color, and the average response is shown in black. A clear response in *Dst* is seen in the first hour of the storm time injection events. The isolated injection events produce no significant *Dst* response.

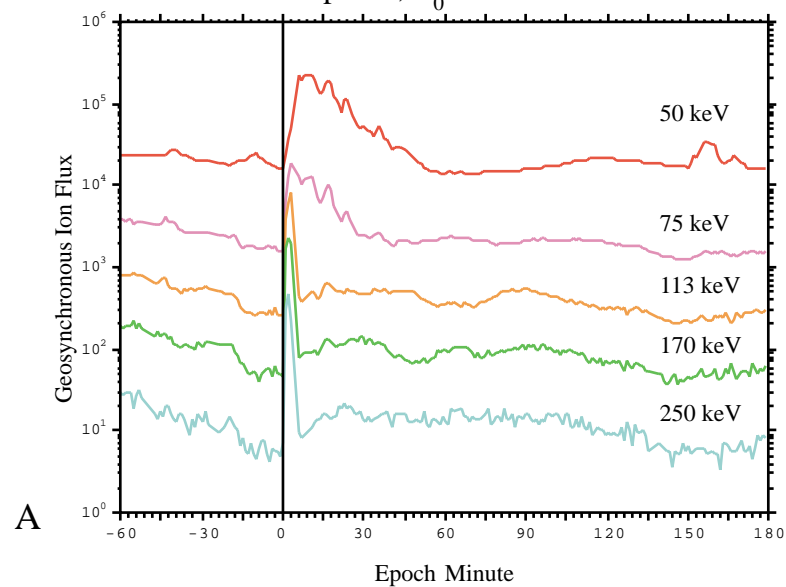
Plate 4. “Composite” energetic neutral atom (ENA) images produced from (a-d) the seven isolated injections and (e-h) the seven storm time injections. Four images are shown, at 1-hour resolution, for each set of events. The ENA fluxes are very similar in the time before and shortly after onset. At times greater than 1 hour after onset the isolated injections show the expected drift and dispersion while during the storms the ENA fluxes intensify and spread east (opposite to the expected ion drift direction) as well as west.

Plate 5. A model calculation of the percentage of ENA emissions originating within $1 R_E$ of the solar-magnetospheric (SM) equatorial plane relative to the ENA emissions from the entire volume of the magnetosphere. In the region from 2 to $6 R_E$ the percentage exceeds 50%, making it a reasonable approximation to assume that the observed ENA fluxes can be mapped to a common reference plane at the equator.

Figure 1. An illustration of the composite imaging technique applied to an image of Abraham Lincoln. (a) A single 15×15 pixel image. (b) Two superposed 15×15 pixel images. (c) Nine superposed 15×15 pixel images.

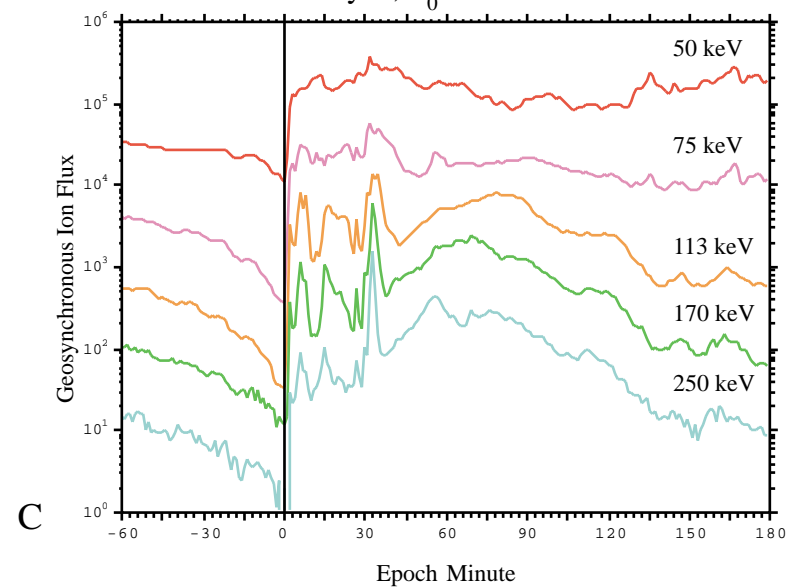
Isolated Injections

April 9, $T_0 = 1444$ UT

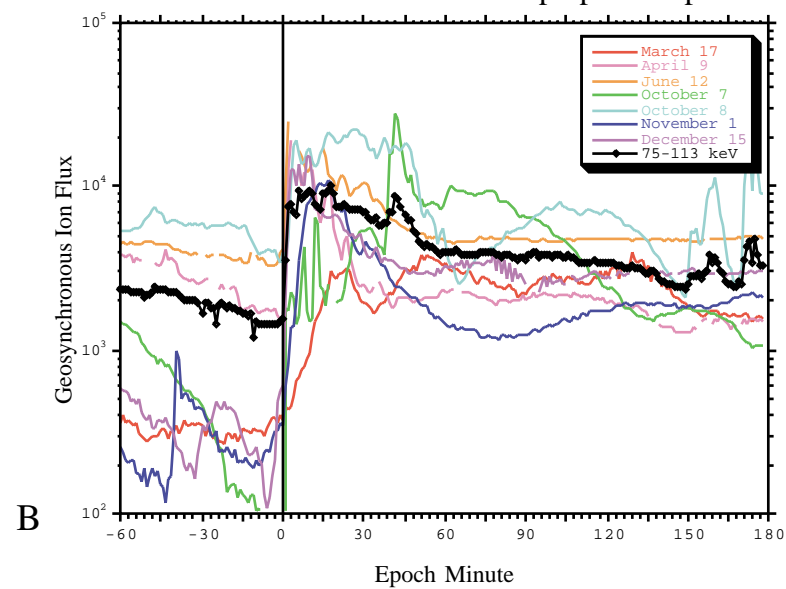


Storm-Time Injections

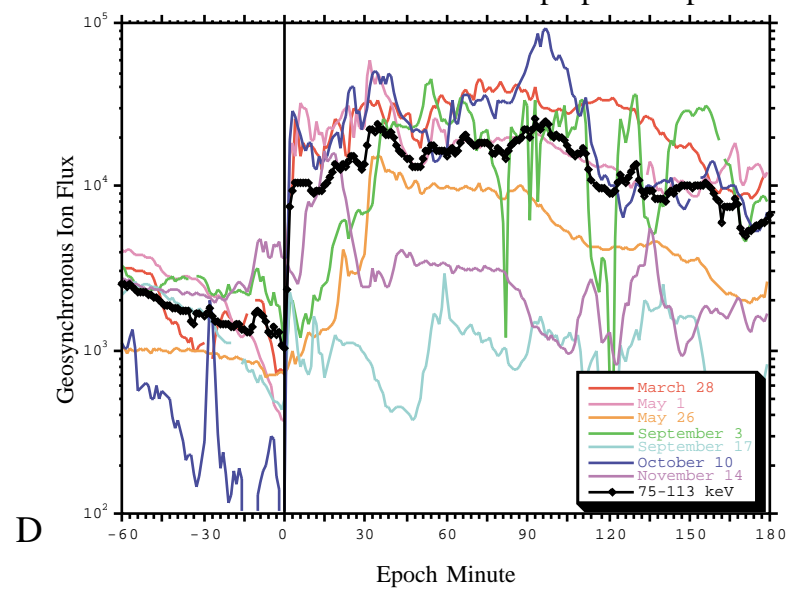
May 1, $T_0 = 1710$ UT



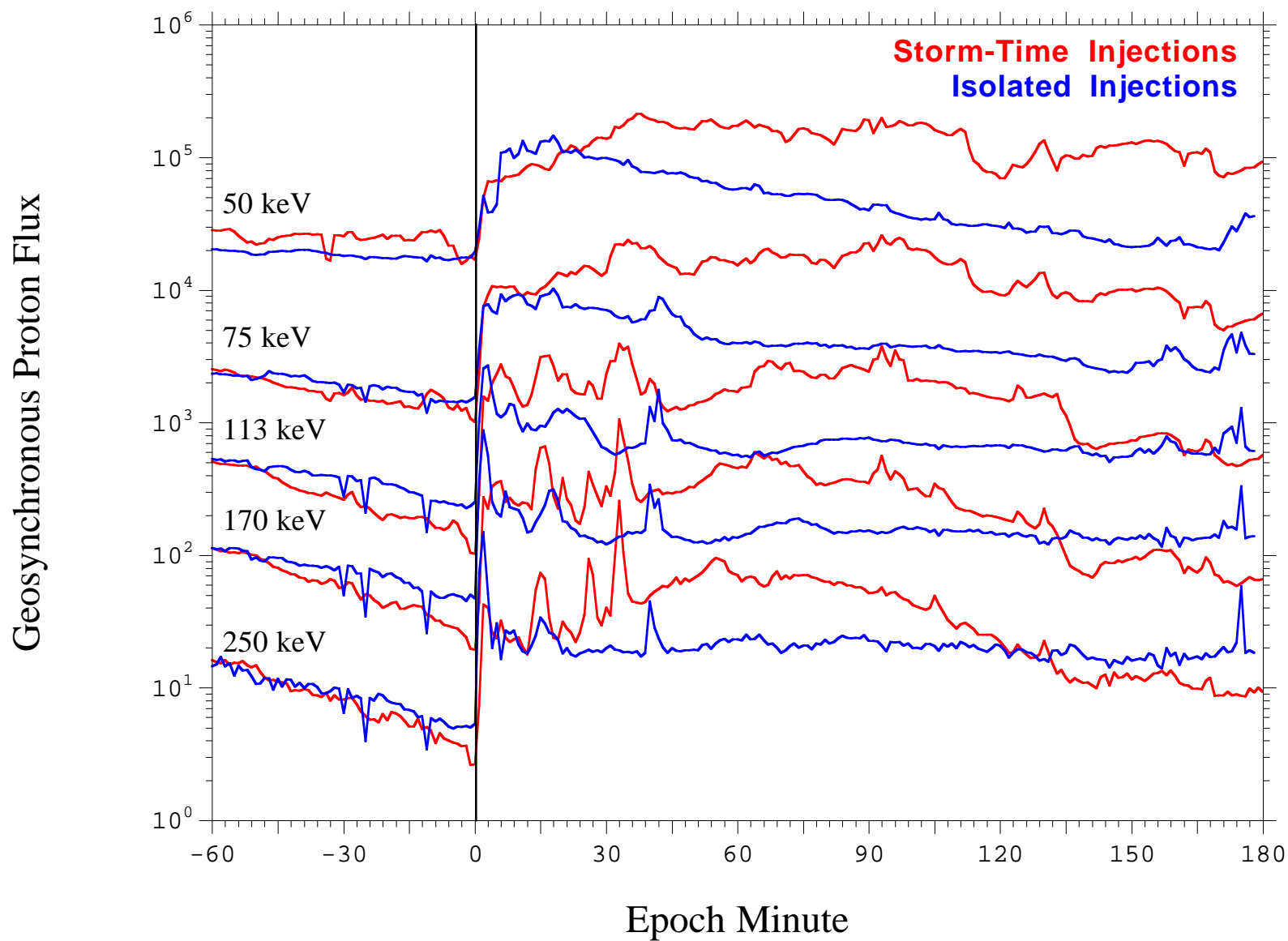
LANL 75-113 keV Proton Superposed Epoch



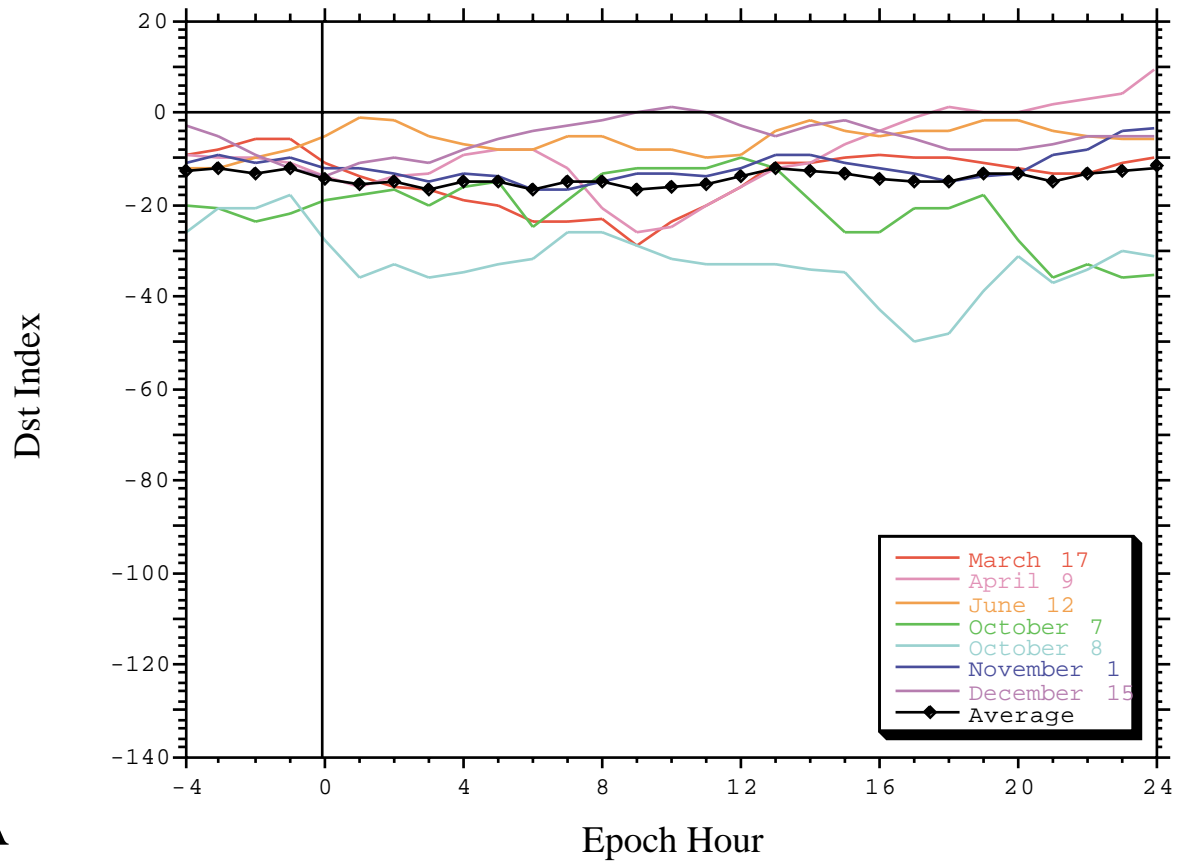
LANL 75-113 keV Proton Superposed Epoch



LANL Proton Superposed Epoch

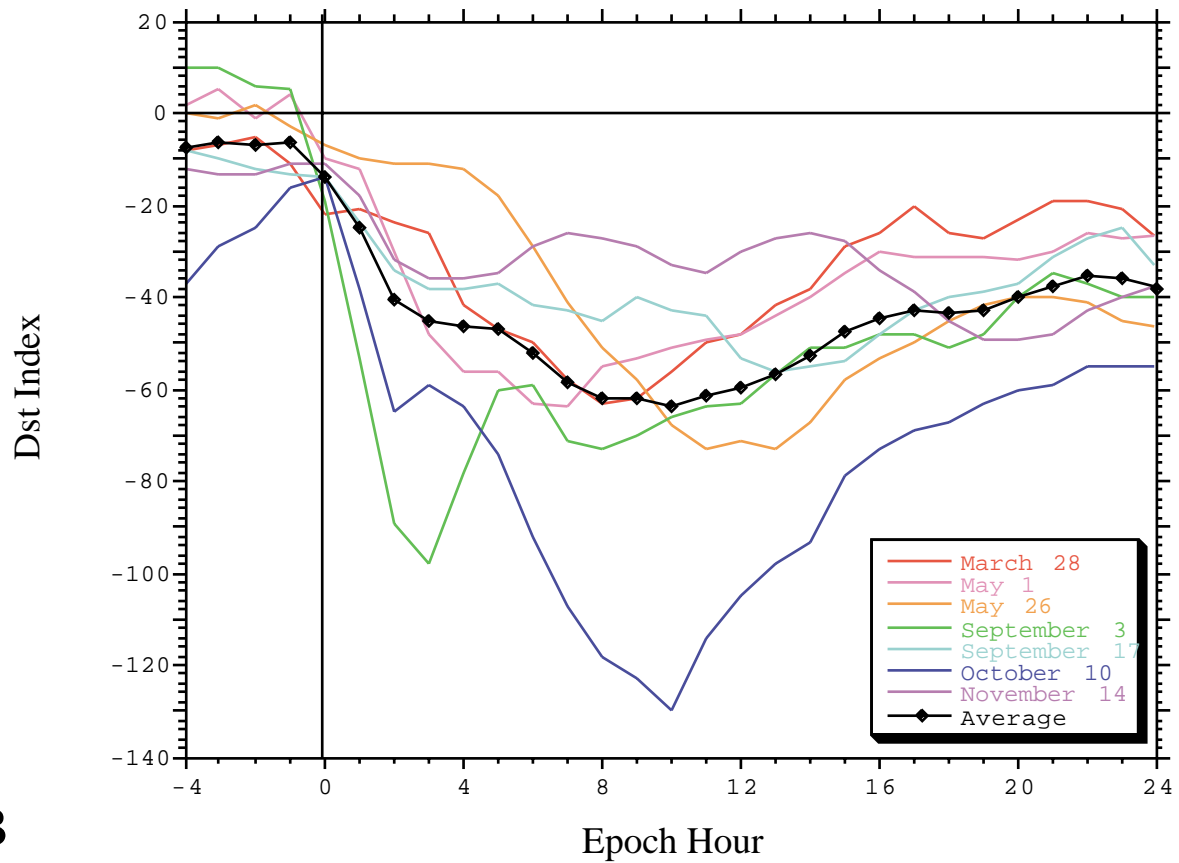


Isolated Injections



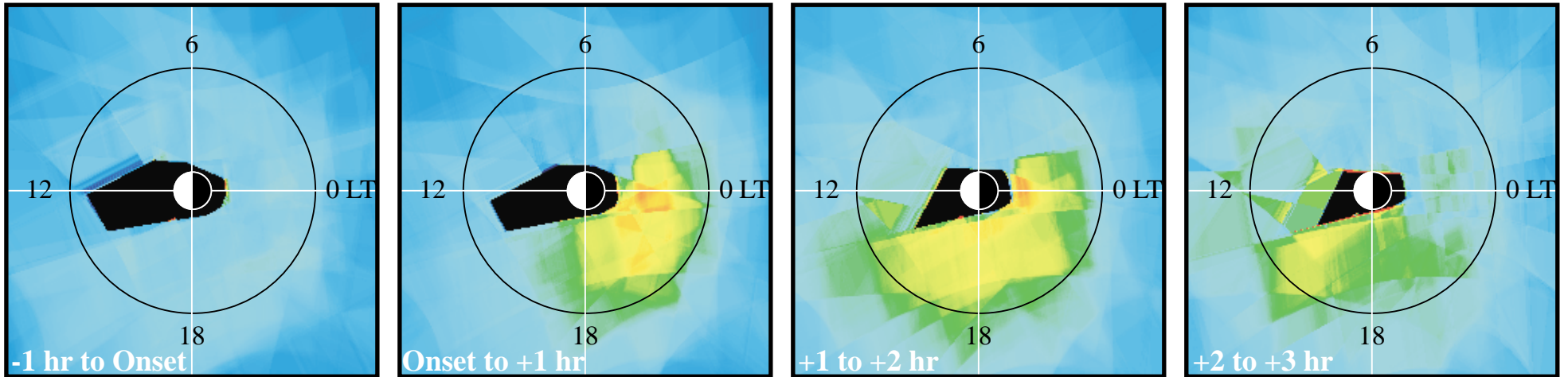
A

Storm-Time Injections

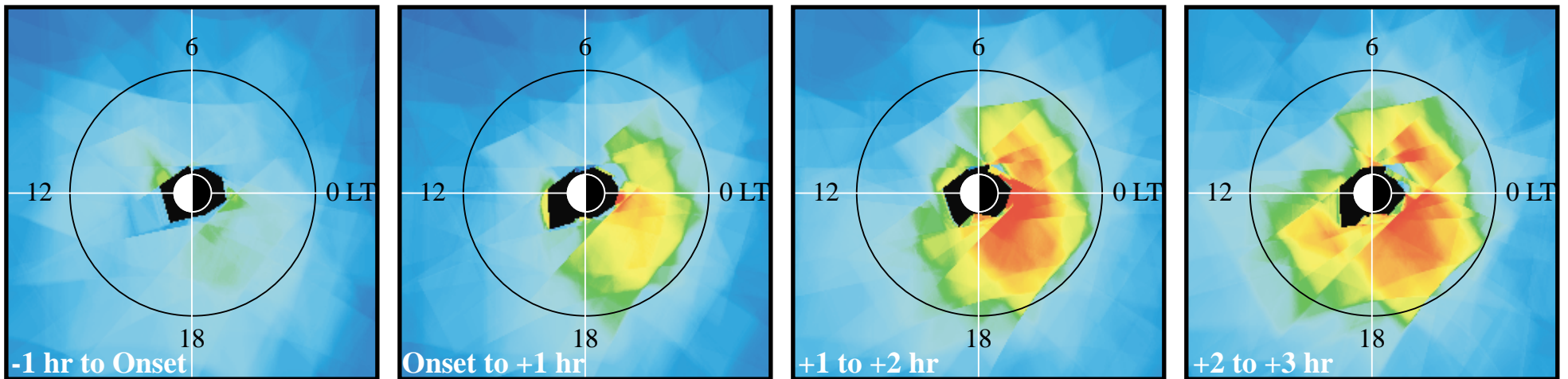


B

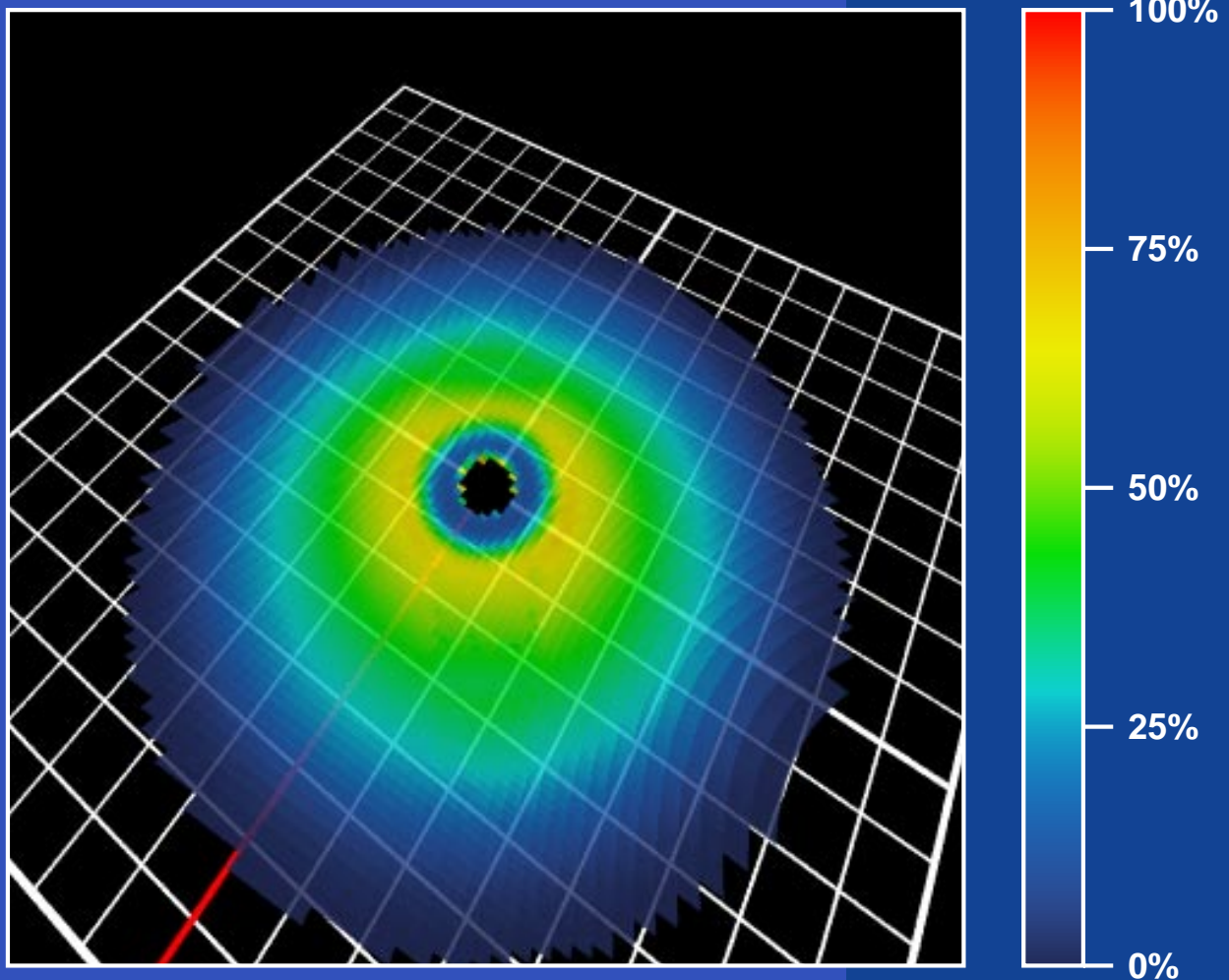
Isolated Injections

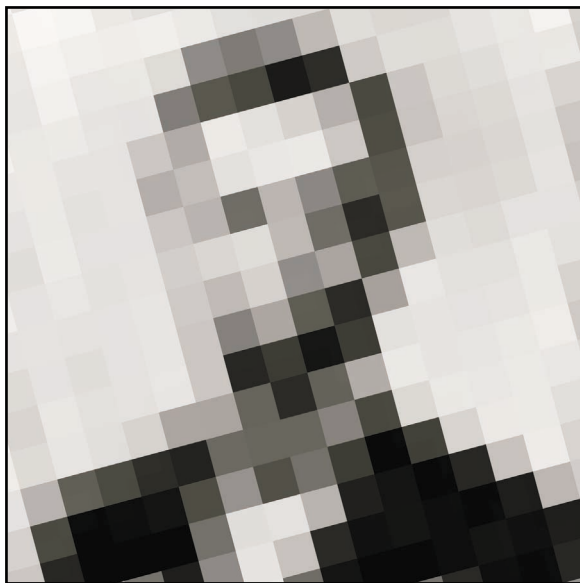


Storm-Time Injections

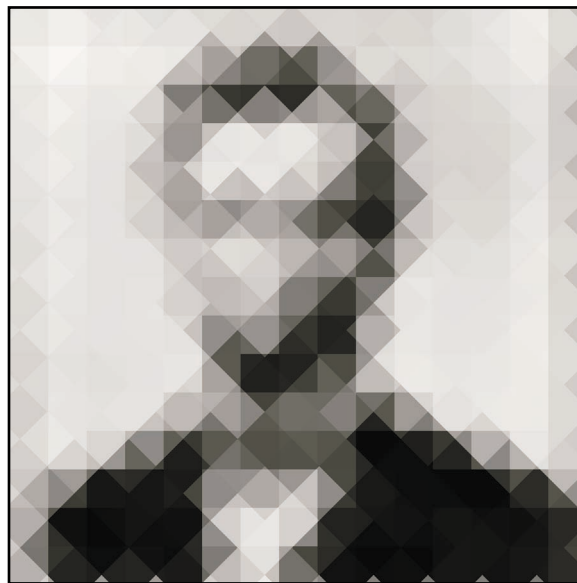


Percentage of ENAs Coming From the $-1 < z < 1$ Slab

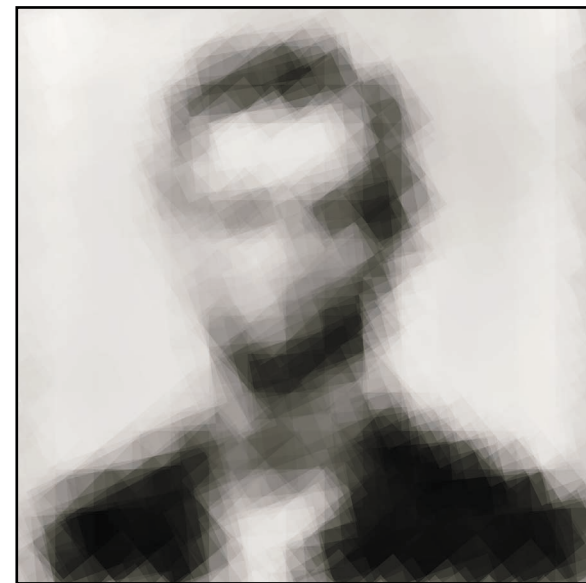




A



B



C

Figure 1